Monthly Notices
of the
ROYAL ASTRONOMICAL SOCIETY

MNRAS **457,** 3448–3456 (2016) doi:10.1093/mnras/stw008

The discovery, monitoring and environment of SGR J1935+2154

G. L. Israel,[1⋆] P. Esposito,[2,3] N. Rea,[4,5] F. Coti Zelati,[4,6,7] A. Tiengo,[8,9,10] S. Campana,[7] S. Mereghetti,[8] G. A. Rodriguez Castillo,[1] D. Götz,[11] M. Burgay,[12] A. Possenti,[12] S. Zane,[13] R. Turolla,[14,13] R. Perna,[15] G. Cannizzaro[16] and J. Pons[17]

[1]*Osservatorio Astronomico di Roma, INAF, via Frascati 33, I-00040 Monteporzio Catone, Italy*
[2]*Istituto di Astrofisica Spaziale e Fisica Cosmica – Milano, INAF, via E. Bassini 15, I-20133 Milano, Italy*
[3]*Harvard-Smithsonian Center for Astrophysics, 60 Garden Street, Cambridge, MA 02138, USA*
[4]*Anton Pannekoek Institute for Astronomy, University of Amsterdam, Postbus 94249, NL-1090-GE Amsterdam, the Netherlands*
[5]*Instituto de Ciencias de l'Espacio (ICE, CSIC–IEEC), Carrer de Can Magrans, S/N, E-08193, Barcelona, Spain*
[6]*Università dell'Insubria, via Valleggio 11, I-22100 Como, Italy*
[7]*INAF – Osservatorio Astronomico di Brera, via Bianchi 46, I-23807 Merate (LC), Italy*
[8]*INAF – Istituto di Astrofisica Spaziale e Fisica Cosmica, via E. Bassini 15, I-20133 Milano, Italy*
[9]*IUSS – Istituto Universitario di Studi Superiori, piazza della Vittoria 15, I-27100 Pavia, Italy*
[10]*INFN – Istituto Nazionale di Fisica Nucleare, Sezione di Pavia, via A. Bassi 6, I-27100 Pavia, Italy*
[11]*AIM CEA/Irfu/Service d'Astrophysique, Orme des Merisiers, F-91191 Gif-sur-Yvette, France*
[12]*Osservatorio Astronomico di Cagliari, via della Scienza 5, I-09047, Cagliari, Italy*
[13]*Mullard Space Science Laboratory, University College London, Holmbury St. Mary, Dorking, Surrey RH5 6NT, UK*
[14]*Dipartimento di Fisica e Astronomia, Università di Padova, via F. Marzolo 8, I-35131 Padova, Italy*
[15]*Department of Physics and Astronomy, Stony Brook University, Stony Brook, NY 11794, USA*
[16]*Università di Roma "La Sapienza", P.le A. Moro 5, I-00185, Roma, Italy*
[17]*Departament de Fisica Aplicada, Universitat d' Alacant, Ap. Correus 99, E-03080 Alacant, Spain*

Accepted 2015 December 31. Received 2015 December 31; in original form 2015 November 3

ABSTRACT

We report on the discovery of a new member of the magnetar class, SGR J1935+2154, and on its timing and spectral properties measured by an extensive observational campaign carried out between 2014 July and 2015 March with *Chandra* and *XMM–Newton* (11 pointings). We discovered the spin period of SGR J1935+2154 through the detection of coherent pulsations at a period of about 3.24 s. The magnetar is slowing down at a rate of $\dot{P} = 1.43(1) \times 10^{-11}$ s s^{-1} and with a decreasing trend due to a negative $\ddot{P}$ of $-3.5(7) \times 10^{-19}$ s s^{-2}. This implies a surface dipolar magnetic field strength of $\sim 2.2 \times 10^{14}$ G, a characteristic age of about 3.6 kyr and a spin-down luminosity $L_{sd} \sim 1.7 \times 10^{34}$ erg s^{-1}. The source spectrum is well modelled by a blackbody with temperature of about 500 eV plus a power-law component with photon index of about 2. The source showed a moderate long-term variability, with a flux decay of about 25 per cent during the first four months since its discovery, and a re-brightening of the same amount during the second four months. The X-ray data were also used to study the source environment. In particular, we discovered a diffuse emission extending on spatial scales from about 1 arcsec up to at least 1 arcmin around SGR J1935+2154 both in *Chandra* and *XMM–Newton* data. This component is constant in flux (at least within uncertainties) and its spectrum is well modelled by a power-law spectrum steeper than that of the pulsar. Though a scattering halo origin seems to be more probable we cannot exclude that part, or all, of the diffuse emission is due to a pulsar wind nebula.

Key words: stars: magnetars – stars: neutron – X-rays: bursts – X-rays: individual: SGR J1935+2154.

1 INTRODUCTION

Large observational and theoretical efforts have been devoted in the past years to unveil the nature of a sample of peculiar high-energy pulsars, namely the anomalous X-ray pulsars and the soft gamma-ray repeaters (SGRs). These objects are believed to be isolated

⋆ E-mail: gianluca@oa-roma.inaf.it

neutron stars and powered by their own magnetic energy, stored in a superstrong field, and are collectively referred to as magnetars (Duncan & Thompson 1992; Paczynski 1992). They share similar timing properties (spin period P in the 2–12 s range and period derivative $\dot{P}$ in the 10^{-13}–10^{-11} s s^{-1} range). Their X-ray luminosity, typically $L_X \sim 10^{33}$–10^{35} erg s^{-1}, generally exceeds the rotational energy-loss rate, while the temperatures of the thermal component observed in their spectra are often higher than those predicted by models of non-magnetic cooling neutron stars. Their (surface dipolar) magnetic fields inferred from the dipolar-loss formula are generally of the order of B$\sim 10^{14}$–10^{15} G. However, recently low dipole field magnetars have been discovered, which behave as typical magnetars but with dipolar magnetic field as low as 6×10^{12} G, i.e. in the range of normal radio pulsars (Rea et al. 2010): these sources possibly store large magnetic energy in other components of their magnetic field (Turolla et al. 2011; Rea et al. 2013).

Sporadically, magnetars emit high-energy (up to the MeV range) bursts and flares which can last from a fraction of a second to minutes, releasing $\sim 10^{38}/10^{47}$ erg s^{-1}, often accompanied by long-lived (up to years) increases of the persistent X-ray luminosity (outbursts). These events may be accompanied or triggered by deformations or fractures of the neutron star crust and/or local/global rearrangements of the star magnetic field. The detection of these energetic events provides the main channel to identify new objects of this class.

A fundamental question about magnetar concerns their evolutionary link to their less magnetic siblings, the rotation-powered pulsars. A number of unexpected results, both from known and newly discovered magnetars, drastically changed our understanding of these objects. In 2004, while studying the emission properties of the bright X-ray transient magnetar XTE J1810-197, the source was discovered to be a bright transient radio pulsar, the first of the class (Camilo et al. 2006). Today we know that 4 out of the about 25 known magnetars are occasionally shining as radio pulsars in the outburst phase. All the radio 'active' magnetars are characterized by a quiescent X-ray over spin-down luminosity ratio of $L_X/L_{sd} < 1$ (Rea et al. 2012).

Energetic pulsars are known to produce particle outflows, often resulting in spectacular pulsar wind nebulae (PWNe) of which the Crab is the most famous example (Weisskopf et al. 2000). Magnetars are expected to produce particle outflows as well, either in quiescence or during outbursts accompanying bright bursts. Given the strong magnetic fields associated with this class of neutron stars, the idea of a wind nebula around a magnetar is thus promising. There has not been yet a confirmed detection of such a nebula, but some cases of 'magnetically powered' X-ray nebulae around pulsars with relatively high magnetic fields have been suggested. A peculiar extended emission has been reported around the rotating radio transient RRAT J1819−1458 (Rea et al. 2009a; Camero-Arranz et al. 2013), with a nominal X-ray efficiency $\eta_X \sim 0.2$, too high to be only rotationally powered. The authors suggested that the occurrence of the nebula might be connected with the high magnetic field (B = 5×10^{13} G) of the pulsar. Similarly, Younes et al. (2012) reported the discovery of a possible wind nebula around Swift J1834−0846, with an X-ray efficiency $\eta_X \sim 0.7$ (but see Esposito et al. 2013 for a different interpretation in terms of dust scatter).

SGR J1935+2154 is a newly discovered member of the magnetar family, and was discovered thanks to the detection of low-Galactic latitude short bursts by *Swift* on 2014 July 5 (Stamatikos et al. 2014). Follow-up observations carried out by *Chandra* on 2014 July 15 and 29 allowed us to precisely locate the source and detect its spin period ($P = 3.25$ s; Israel et al. 2014) confirming that SGR J1935+2154 is indeed a magnetar. The SGR J1935+2154 position is coincident with the centre of the Galactic supernova remnant (SNR) G57.2+0.8 of undetermined age and at a possible, but uncertain, distance of 9 kpc (Sun et al. 2011; Pavlović et al. 2013).

In this paper, we report on the results of an *XMM–Newton* and *Chandra* observational campaign covering the first eight months of SGR J1935+2154's outburst. Our observational campaign is ongoing with *XMM–Newton*, and its long-term results will be reported elsewhere. We also report upper limits on the radio emission derived from Parkes observations (Burgay et al. 2014). We first report on the data analysis, then summarize the results we obtained for the parameters, properties and environment of this new magnetar. Finally, we discuss our findings in the contest of the magnetar scenario.

Table 1. Summary of the *Swift*, *Chandra* and *XMM–Newton* observations used in this work and carried out between 2014 July and 2015 March.

Mission / Obs. ID	Instrument	Date	Exposure (ks)
Swift/603488000	XRT	July 5	3.4
Swift/603488002	XRT	July 6	4.3
Swift/603488004	XRT	July 7	9.3
Swift/603488006	XRT	July 8	3.7
Swift/603488008	XRT	July 13	5.3
Swift/603488009	XRT	July 13	3.0
Chandra/ 15874	ACIS-S	July 15	10.1
Swift/603488010	XRT	July 16	7.1
Chandra/ 15875	ACIS-S[a]	July 28	75.4
Chandra/ 17314	ACIS-S[a]	August 31	29.2
XMM / 0722412501	EPIC	September 26	19.0
XMM / 0722412601	EPIC	September 28	20.0
XMM / 0722412701	EPIC	October 04	18.0
XMM / 0722412801	EPIC	October 16	9.7
XMM / 0722412901	EPIC	October 24	7.3
XMM / 0722413001	EPIC	October 27	12.6
XMM / 0748390801	EPIC	November 15	10.8
XMM / 0764820101	EPIC	March 25	28.4

[a]Data collected in continuous clocking mode (CC).

2 X-RAY OBSERVATIONS

2.1 *Chandra*

Chandra observations of SGR J1935+2154 were carried out three times during 2014 July and August (see Table 1) in response to the detection of short SGR-like bursts from the source. The first data set was acquired with the ACIS-S instrument in Faint imaging (Timed Exposure) and 1/8 sub-array mode (time resolution: ∼0.44 s), while the subsequent two pointings were obtained with the ACIS-S in Faint timing (Continuous Clocking) mode (time resolution 2.85 ms).

The data were reprocessed with the Chandra Interactive Analysis of Observations software (CIAO, version 4.6) using the calibration files available in the *Chandra* CALDB 4.6.3 data base. The scientific products were extracted following standard procedures, but adopting extraction regions with different size in order to properly subtract the underlying diffuse component (see Section 3.2 and Fig. 1). Correspondingly, for the first observation (Faint imaging) we used circular regions of 1.5 arcsec (and 3.0 arcsec) radius for the source (and diffuse emission) associated with a background annular region with 1.6 and 3.0 arcsec (10 arcsec, 15 arcsec) for the inner and outer radius, respectively. Furthermore, we used rectangular boxes of 3 arcsec × 2 arcsec (and 4 arcsec × 2 arcsec) sides aligned to the CCD readout direction for the remaining two observations

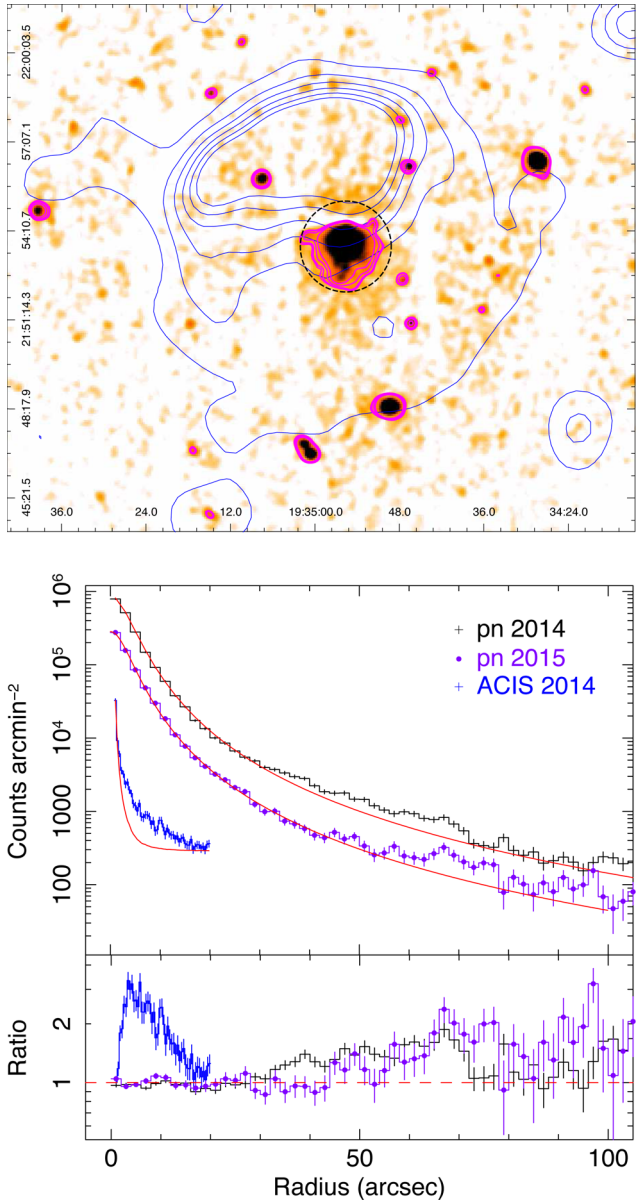

Figure 1. Top: 98 ks-long *XMM–Newton* PN image of the region around SGR J1935+2154; the 1.4 GHz radio map of SNR G57.2+0.8 is also shown (blue contours from the VLA Galactic Plane Survey; Stil et al. 2006, upper image). The *XMM–Newton* image has been smoothed with a Gaussian function with a radius of 4 arcsec and magenta contours are displayed in order to emphasize the extended emission around SGR J1935+2154. The black dashed circle marks a distance of 90 arcsec from the SGR J1935+2154 position. Bottom: 2014 and 2015 *XMM–Newton* and *Chandra* surface brightness (black crosses, purple squares and blue crosses, respectively) as a function of the distance from SGR J1935+2154 compared with their point spread functions (PSF, red lines, lower plot). The ratios between the data and the PSF are plotted in the lowest panel.

in continuous clocking (CC) mode. For the background, we used two rectangular boxes of 1.5 arcsec × 1.5 arcsec (and 2 arcsec × 2 arcsec) at the sides of the source extraction region. For the spectra, the redistribution matrices and the ancillary response files were created using SPECEXTRACT. For the timing analysis, we applied the Solar system barycentre correction to the photon arrival times with AXBARY.

2.2 *XMM–Newton*

XMM–Newton observations of SGR J1935+2154 were carried out between 2015 September and March (see Table 1) to monitor the source decay and study the source properties. We used the data collected with the European Photon Imaging Camera (EPIC), which consists of two Metal Oxide Semi-conductor (MOS) (Turner et al. 2001) and one pn (Strüder et al. 2001) CCD detectors. The raw data were reprocessed using the *XMM–Newton* Science Analysis Software (SAS, version 14.0) and the calibration files in the CCF release of 2015 March. The pn operated in Full Window (time resolution of about 73 ms) while the MOSs were set in Small Window (time resolution of 300 ms), therefore optimized for the timing analysis. The intervals of flaring background were located by intensity filters (see e.g. De Luca & Molendi 2004) and excluded from the analysis. Source photons were extracted from circles with radius of 40 arcsec. The pn background was extracted from an annular region with inner and outer radii of 45 and 90 arcsec, respectively (also in this case the choice was dictated by the diffuse emission component, Section 3.2 and Fig. 1). Photon arrival times were converted to the Solar system barycenter using the SAS task BARYCEN using the source coordinate as inferred from the *Chandra* pointings (see Section 3.1). The ancillary response files and the spectral redistribution matrices for the spectral analysis were generated with ARFGEN and RMFGEN, respectively. In order to maximize the signal-to-noise ratio we combined, when needed, the spectra from the available EPIC cameras and averaged the response files using EPICSPECCOMBINE. In particular, the latter command was routinely applied for the study of the dim diffuse emission.

2.3 *Swift*

The *Swift* X-Ray Telescope (XRT) uses a front-illuminated CCD detector sensitive to photons between 0.2 and 10 keV (Burrows et al. 2005). Two readout modes can be used: photon counting (PC) and windowed timing (WT). The PC mode provides images and a 2.5 s time resolution; in WT mode only 1D imaging is preserved with a time resolution of 1.766 ms. Data were processed with XRTPIPELINE (version 12), and altered and screened with standard criteria, correcting for effective area, dead columns, etc. Events were extracted from a 20 pixel radius region around the source position. For spectroscopy, we used the spectral redistribution matrices in CALDB (20130101, v014 for the PC), while the ancillary response les were generated with XRTMKARF.

3 ANALYSIS AND RESULTS

3.1 Position

We used the *Chandra* ACIS-S observation carried out on 2014 July 15, the only one in imaging mode, in order to precisely locate SGR J1935+2154. Only one bright source was detected in the S7 CCD operating at one-eighth of the nominal field of view. The refined position of the source, calculated with WAVDETECT, is RA = $19^{\rm h}34^{\rm m}55\overset{\rm s}{.}5978$, Dec. = $+21^\circ53'47\overset{''}{.}7864$ (J2000.0, statistical uncertainty of 0.02 arcsec) with a 90 per cent confidence level uncertainty radius of 0.7 arcsec. This position is consistent with that of SGR J1935+2154 obtained by *Swift*: RA = $19^{\rm h}34^{\rm m}55\overset{\rm s}{.}68$, Dec. = $+21^\circ53'48\overset{''}{.}2$, J2000.0, radius of 2.3 arcsec at 90 per cent confidence level (Cummings et al. 2014). Correspondingly, we are confident that the source we detected in the *Chandra* image is indeed the source first detected by *Swift* Burst Alert Telescope (BAT) and later by XRT and responsible for the observed SGR-like bursts.

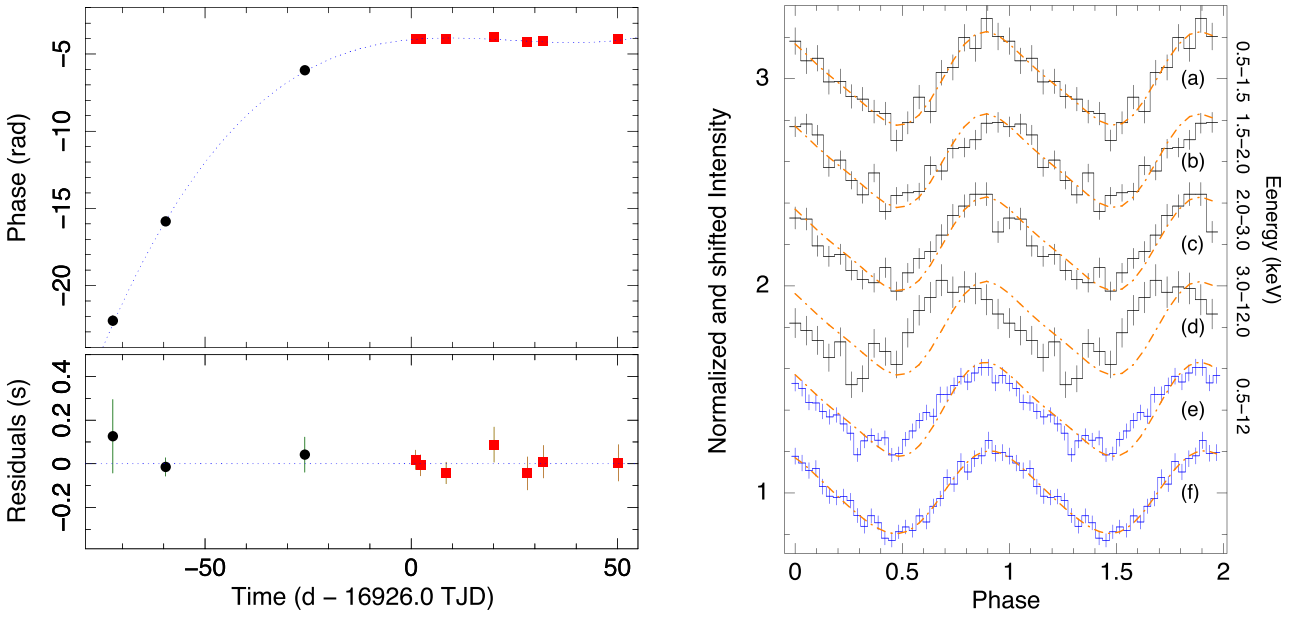

Figure 2. Left: SGR J1935+2154's phase evolution as a function of time fitted with a linear plus a quadratic plus a cubic components (upper panel). The residuals with respect to our best phase-coherent solution are reported in the lower panel, in units of seconds. Black circle and red square points mark the *Chandra* and *XMM–Newton* observations, respectively. Right: *Chandra* plus *XMM–Newton* background-subtracted pulse profiles (arbitrary shifted on the *y*-axis). From top to bottom, they refer to: (a) 0.5–1.5 keV, (b) 1.5–2.0 keV, (c) 2.0–3.0 keV, (d) 3.0–12.0 keV and (e) 0.5–12.0 keV. The dashed orange curve marks the best fit (by assuming a model with two sinusoids) of profile (a): a systematic shift towards smaller phases (advance in time) as a function of energy is evident. Profile (f) has been obtained by aligning profiles from (a) to (d).

3.2 Spatial analysis

Upon visual inspection of the X-ray images, it is apparent that SGR J1935+2154 is embedded in a patch of diffuse emission. To assess this in detail, we built for each pn observation a radial profile in the 0.4–10 keV band and fit a point spread function (approximated by a King model; Read et al. 2011) to it. In each instance, the inner part of the profile can be fit by a King model with usual core radius and slope values, whereas at radii ≈30–40 arcsec, the data start to exceed significantly the model prediction. Since we obtained consistent results from all the 2014 observations, we repeated the same analysis on the stacked images in order to improve the signal-to-noise ratio of the data. We also selected the photons in the 1–6 keV energy range, since the spectral analysis (see Section 3.4) shows that the diffuse emission is more prominent in this band. The combined 2014 *XMM–Newton* profile is shown in black in Fig. 1. The diffuse emission emerges at $\gtrsim$30 arcsec from SGR J1935+2154 and extends to at least 70 arcsec. It is however not possible to determine where the feature ends, because of both the low signal to noise ratio at large distance from the point source and the gaps between the CCDs. The profile of the latest *XMM–Newton* data set has been obtained separately from the remaining data sets in order to look for shape variabilities of the diffuse component on long time-scales. The two pn profiles are in agreement within the uncertainties (determined by using a Kolmogorov–Smirnov test that there is a substantial probability (>50 per cent) that the two profiles have been extracted from the same distribution), though a possible shift of the diffuse component, towards larger radii, might be present in the 30–40 arcsec radius interval.

A similar analysis was carried out by using the longest *Chandra* data set. Though the latter is in CC mode, the field is not particularly crowded and only faint point-like objects are detected in the field of view. Correspondingly, it is still possible to gather information over smaller scales than in the *XMM–Newton* data. The ACIS-S PSF was simulated using the Chandra Ray Tracer (ChaRT) and Model of *AXAF* Response to X-rays (MARX v5.0.0-0) software packages.[1] The result of this analysis is shown in blue in Fig. 1. Diffuse emission is clearly present in the *Chandra* data and starts becoming detectable at a distance of >1 arcsec from the source. Due to poor statistics we have no meaningful information at radii larger than ∼15 arcsec. Therefore, we are not able to assess if the diffuse structures detected by *XMM–Newton* and *Chandra* are unrelated to each other or linked somehow.

3.3 Timing analysis

The 0.5–10 keV events were used to study the timing properties of the pulsar. The average count rate obtained from *Chandra* and *XMM–Newton* was 0.11 ± 0.02 and 0.21 ± 0.01 cts s^{-1}, respectively. Coherent pulsations at a period of about 3.24 s were first discovered in the 2014 July 29 *Chandra* data set carried out in CC mode (Israel et al. 2014). The pulse shape is nearly sinusoidal and does not show variations as a function of time. Also the pulsed fraction, defined as the semi-amplitude of the sinusoid divided by the source average count rate, is time independent (within uncertainties) and in the 17/21 per cent range (1σ uncertainty of about 1.5 per cent). Additionally, the pulse shape does not depend on the energy range, though a shift in phase of about 0.16 cycles is clearly detected between the soft (0.5–1.5 keV) and hard (3.0–12.0 keV) energy bands, with hard photons anticipating the soft ones (see Fig. 2).

A refined value of $P = 3.244\,978(6)$ s ($1\,\sigma$ confidence level; epoch 56866.0 MJD) was inferred based on a phase-coherent analysis. Due to the long time elapsed between the epoch of the first period

[1] For more details on the tasks, see http://cxc.harvard.edu/chart/index.html and http://space.mit.edu/cxc/marx/index.html

Table 2. Timing results.

Epoch T_0 (MJD)	56926.0
Validity range (MJD)	56853.6–56976.4
$P(T_0)$ (s)	3.245 0650(1)
$\dot{P}(T_0)$	$1.43(1) \times 10^{-11}$
$\ddot{P}(T_0)$ (s^{-1})	$-3.5(7) \times 10^{-19}$
$\nu(T_0)$ (Hz)	0.308 160 23(1)
$\dot{\nu}(T_0)$ (Hz s^{-1})	$-1.360(3) \times 10^{-12}$
$\ddot{\nu}(T_0)$ (Hz s^{-2})	$3.3(7) \times 10^{-20}$
rms residual (ms)	55
χ^2_ν (dof)	0.57 (6)
B_p (Gauss)	2.2×10^{14}
τ_c (yr)	3600
L_{sd} (erg s^{-1})	1.7×10^{34}

determination and those of the other *Chandra* observations, we were not able to furthermore extend the timing solution based on the *Chandra* data. Therefore, we inferred a new phase-coherent solution by means of the seven *XMM–Newton* pointings carried out between the end of 2014 September and mid-November (red filled circles in left-hand panel of Fig. 2). The new solution also included a first period derivative component: $P = 3.245\,0656(2)$ s and $\dot{P} = 1.37(3) \times 10^{-11}$ s s^{-1} (1σ confidence level; epoch 56926.0 MJD, χ^2 of 3.1 for 4 dof).

The latter timing solution was accurate enough to include the previous *Chandra* pointings (black filled circles in left-hand panel of Fig. 2). The final timing solution, encompassing the whole data set, is reported in Table 2 and includes a second period derivative acting in the direction of decelerating the rate of period change $\dot{P}$. The inclusion of the new $\ddot{P}$ component has a F-test probability of 8×10^{-4} and 10^{-7} of not being needed (when considering only the *XMM–Newton* data sets or the whole 10 pointings in the fit, respectively). Moreover, the new timing solution implies a rms variability of only 55 ms, corresponding to a timing noise level of less than 2 per cent, well within the value range observed in isolated neutron stars.

We note that the second period derivative we found is unlikely to result from a change, as a function of time, of the pulse profiles, which are almost sinusoidal and show no evidence for variation (see right-hand panel of Fig. 2).

We notice that this analysis is valid under the assumption that the location and geometry of the emitting region remains constant throughout the observations, as suggested by studies of other transient magnetars (see Perna & Gotthelf 2008; Albano et al. 2010).

The accuracy of the timing solution reported in Table 2 is not good enough to coherently include the 2015 March *XMM–Newton* data. Correspondingly, we inferred the period for this latest pointing similarly to what reported above finding a best value of $P = 3.245\,28(6)$ s (95 per cent confidence level, epoch 57106.0 MJD). This is less than 2σ away from the expected period extrapolated from the timing solution in Table 2. The pulse profile parameters changed significantly with respect to the previous data sets with a pulsed fraction of only 5 ± 1 per cent (1σ) and a more asymmetric shape.

3.4 Spectral analysis

For the phase-averaged spectral analysis (performed with XSPEC 12.8.2 fitting package; Arnaud 1996), we started by considering all the data sets together. Then, we concentrated on the 2014 July 29 data, being the longest and highest statistics *Chandra* pointing (about 75 ks effective exposure for 8200 photons) and the *XMM–Newton* pn spectra (effective exposure time of about 105 ks and 22 000 events). A summary of the spectral fits is given in Table 3. To account for the above reported diffuse component (see Section 3.2) we used, as background spectra of the point-like central source, the regions we described in Sections 2.1 and 2.2 and from which we extracted later the diffuse component spectra.

We started by fitting all the 10 data sets carried out during 2014 separately leaving free to vary all the parameters. The absorption was forced to be free but the same among observations. Photons having energies below about 0.8 keV and above 10 keV were ignored, owing to the very few counts from SGR J1935+2154 (energy channels were rebinned in a way of having at least 30 events). Furthermore, all the energy channels consistent with zero after the background subtraction were ignored. The abundances used were those of Wilms, Allen & McCray (2000). The spectra were not fitted well by any single component model such as a power-law (PL) or blackbody (BB) which gave a reduced χ^2 in the 1.2–1.8 range depending on the used single component (282 and 407 degrees of freedom, hereafter dof, for the *Chandra* and *XMM–Newton* spectra, respectively). A canonical two-component model often used to model magnetars, i.e. an absorbed BB plus PL, resulted in a good fit with reduced χ^2 of 0.99 (280 dof) and 1.03 (405 dof) for the *Chandra* and *XMM–Newton* spectra, respectively. The inclusion of a furthermore spectral component (the BB in the above procedure) was evaluated to have a formal F-test probability equal to 4.5σ and 7.0σ (for *Chandra* and *XMM–Newton*, respectively) of being significant.

Table 3. *Chandra* and *XMM–Newton* spectral results. Errors are at a 1σ confidence level for a single parameter of interest.

Mission (Model)	N_H[b] (10^{22} cm^{-2})	Γ	kT (keV)	R_{BB} [c] (km)	Flux[d] (10^{-12} erg cm^{-2} s^{-1})	Luminosity[d] (10^{34} erg s^{-1})	χ^2_ν (dof)
			SOURCE EMISSION				
CHANDRA (BB + PL)	2.0 ± 0.4	2.8 ± 0.8	0.45 ± 0.03	1.9 ± 0.2	1.24 ± 0.06	3.1 ± 0.5	0.97 (165)
XMM (BB + PL)	1.6 ± 0.2	1.8 ± 0.5	0.47 ± 0.02	1.6 ± 0.1	0.89 ± 0.05	1.7 ± 0.4	1.02 (74)
XMM[e] "	1.6 ± 0.2	2.1 ± 0.4	0.48 ± 0.02	1.6 ± 0.2	1.19 ± 0.06	2.4 ± 0.5	0.93 (109)
			DIFFUSE EMISSION				
XMM (PL)	3.8 ± 0.4	3.8 ± 0.3	–	–	0.14 ± 0.02	0.6 ± 0.1	1.94 (23)

[a] XSPEC models; BB = BBODYRAD, PL = POWERLAW.
[b] We used the abundances of Wilms et al. (2000).
[c] The blackbody radius is calculated at infinity and for an arbitrary distance of 9 kpc.
[d] In the 1–10 keV energy band; fluxes are observed values, luminosities are de-absorbed quantities.
[e] 2015 March *XMM–Newton* observation.

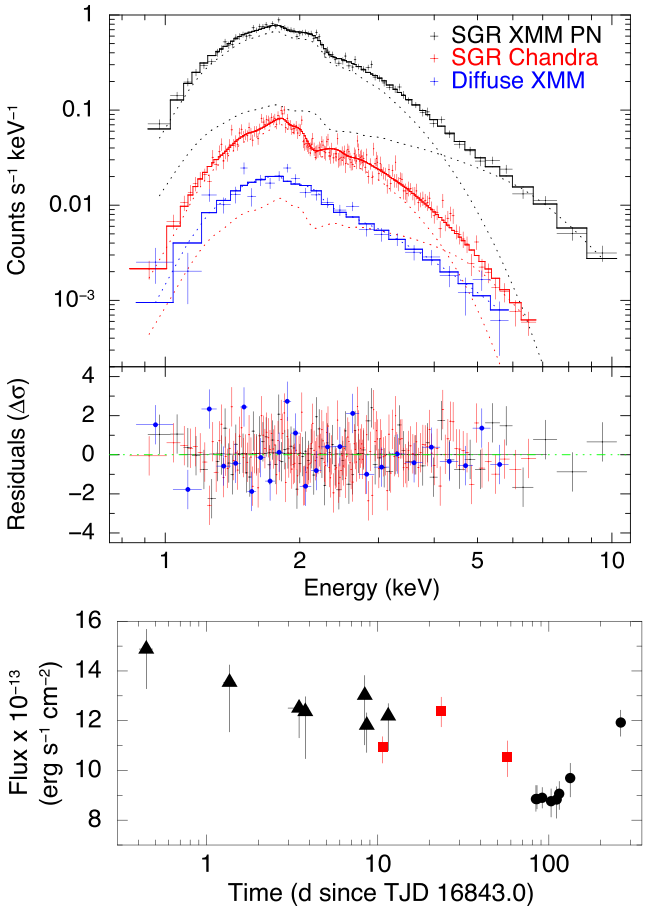

Figure 3. Spectra of SGR J1935+2154 and of the diffuse emission around the pulsar. From top to bottom: SGR J1935+2154 cumulative *XMM–Newton* PN spectrum, the SGR J1935+2154 *Chandra* ACIS spectrum of observation 15875 and the cumulative *XMM–Newton* PN spectrum of the diffuse emission (upper plot). Residuals (in σ units) are shown and refer to the absorbed PL+BB model for SGR J1935+2154 and to a PL model for the diffuse component. Time evolution for the absorbed 1–10 keV flux of SGR J1935+2154 obtained by using data sets from *Swift* (black triangles), *Chandra* (red squares) and *XMM–Newton* (black circles). The zero on the *x*-axis marks the *Swift* BAT trigger.

A flux variation, of the order of about 25 per cent, was clearly detected between the *Chandra* and *XMM–Newton* 2014 pointings. On the other hand no significant flux variation was detected among spectra of *XMM–Newton* observations. Correspondingly, in order to increase the statistics we proceeded to combine the seven *XMM–Newton* 2014 spectra together (we used the SAS task EPICSPECCOMBINE). By using the latter spectrum, we obtain a F-test probability of 7.8σ that the BB component inclusion is significant. In the upper panel of Fig. 3 the *XMM–Newton* combined source spectrum (in black) is reported together with the *Chandra* spectrum of the longest pointing (in red, the two further *Chandra* spectra are not shown in figure for clarity purposes). We note that, within about 1σ uncertainties, the *Chandra* and *XMM–Newton* spectral parameter are consistent with each other with the exception of the flux.

The latest *XMM–Newton* pointing, carried out in 2015 March, was not combined with the previous ones in order to look for spectral variability on long time-scales. While the PL plus BB spectral decomposition holds also for this data set, the flux significantly increased by about 25 per cent reaching a level similar to that of the longest *Chandra* pointing in 2014 July. It is evident from Table 3 that the only significantly changed parameter is the flux of the PL component.

Due to the poor statistics of the *Swift* XRT spectra, we only inferred the 1–10 keV fluxes by assuming the PL plus BB model obtained by the combined *XMM–Newton* spectrum and including a scale factor which was free to vary in order to track the flux variation through the outburst. The lower panel of Fig. 3 includes all the 1–10 keV observed fluxes inferred from the *Swift*, *Chandra* and *XMM–Newton* spectra. It is evident that the source is still variable above a general decay trend.

The same background regions used to correct the EPIC pn source spectra were then assumed as a reliable estimate of the diffuse emission. For the background of the diffuse emission, we considered two regions lying far away (at a distance >4 arcmin) from the pulsar and in two different CCDs obtaining similar results in both cases. We first fit all the seven spectra together. The use of one spectral component gave a relatively good fit with a reduced χ^2 of 1.22 and 1.33 (107 dof) for an absorbed PL and BB model, respectively. Then we left free to vary all the parameters resulting in a reduced χ^2 of 1.15 and 1.18 (95 dof) for the PL and BB model, respectively. While no improvement was achieved for the BB model, the PL model appears to vary among *XMM–Newton* observations at about 2.0σ confidence level. Therefore, we conclude that there is no suggestion of variability for the diffuse emission. A combined (from the seven *XMM–Newton* pointings) spectrum for the diffuse emission was obtained, in a way similar to that already described for the source spectrum. The *XMM–Newton* combined spectrum of the diffuse emission and the results of the spectral fitting for the PL model are shown in Fig. 3 and in Table 3. Two facts can be immediately evinced: a simple model is not a good approximation for the diffuse emission and the absorbing column is significantly different from the one we inferred for the magnetar. At present stage, we cannot exclude that the two things are related to each other. In particular, we note that the largest values of the residuals originated from few 'random' data points rather than by an up-and-down trend (often suggesting a wrong adopted continuum component, see blue points in the lower panel of Fig. 3). Also for the diffuse emission we kept separated the 2015 *XMM–Newton* observation in order to look for spectral variations. Unfortunately, the low statistics prevented us in checking if changes in the spectral parameters are present. The inferred 1–10 keV observed flux is $(1.67\pm^{0.03}_{0.05}) \times 10^{-13}$ erg cm^{-2} s^{-1}, in agreement with the 2014 value.

3.5 Pre-outburst observations

Swift XRT observed SGR J1935+2154 twice before its activation during the *Swift* Galactic plane survey (see Campana et al. 2014). The first observation took place on 2010 December 30 for 514 s (obsid 00045278001). SGR J1935+2154 is far off-axis (~10 arcmin) and we derived a 3σ upper limit of 3.2×10^{-2} cts s^{-1}.

The second observation took place on 2011 August 28 for 617 s (obsid 00045271001). SGR J1935+2154 is detected at a rate $(1.55 \pm 0.63) \times 10^{-2}$ cts s^{-1}. Assuming the same spectral model of the *XMM–Newton* observations (see Section 3.4 and Table 3), we derive a 1–10 keV luminosity of $(9.3 \pm 3.6) \times 10^{33}$ erg s^{-1} (including uncertainties in the count rate and assuming a distance of 9 kpc).

The field was also imaged during the ROSAT all-sky survey twice, but the high column density prevents any firm upper limit on the observed flux.

Table 4. The table lists for each radio observation: the date and time (UT) of the start of the acquisition (in the form yy-mm-dd-hh:mm); the receiver used, either the 10 cm feed of the coaxial 10–50 cm (Granet et al. 2005) or the central beam of the 20 cm multibeam receiver (Staveley-Smith et al. 1996); the integration time; the flux density upper limit for a pulsed signal with a 3.2 s period; the flux density upper limit for a single pulse of 32 ms duration. Flux are expressed in mJy units.

UT start	Rec	T_{obs} (h)	S_{min}	S^{sp}_{min}
14-08-01-11:34	10–50 cm	3.0	0.04	68
14-08-02-11:22	10–50 cm	3.0	0.04	68
14-08-03-12:29	20 cm-MB	1.5	0.05	61
14-08-03-13:32	10–50 cm	1.0	0.07	68
14-09-28-08:34	10–50 cm	2.0	0.05	68

4 RADIO OBSERVATIONS

The first radio follow-up observations of SGR J1935+2154 were carried out on 2014 July 9 and 14 from the Ooty Radio Telescope and the Giant Meterwave Radio Telescope, at 326.5 and 610.0 MHz, respectively (Surnis et al. 2014). No pulsed radio emission was found down to a flux of 0.4 and 0.2 mJy at 326.5 and 610.0 MHz (assuming a 10 per cent duty cycle), respectively.

The source was observed with the Parkes radio telescope at 10 and 20 cm in four epochs between August 1 and 3, shortly after the detection of X-ray pulsations (Israel et al. 2014), and again at 10 cm on September 28, almost simultaneously with one of our *XMM–Newton* observations. Observations at 10 cm were obtained using the ATNF Digital Filterbanks DFB3 (used in search mode with a sampling time of 1 ms) and DFB4 (in folding mode) at a central frequency of 3100 MHz, over 1024 MHz of bandwidth. 20 cm observations were acquired using the reconfigurable digital backend HIPSR (HI-Pulsar signal processor) with a central frequency of 1357 MHz, a 350 MHz bandwidth and a sampling time of 64 μs. Further details of the observations are summarized in Table 4.

Data were folded in 120 s long sub-integrations using the ephemeris in Table 2 and then searched over a range of periods, spanning ±1.5 ms with respect to the X-ray value of any given observing epoch, and over dispersion measures (DMs) up to 1000 pc cm^{-3}.

The data acquired in search mode were also blindly searched over DMs up to 1000 both for periodic signals and single dedispersed pulses. The 20 cm data were searched in real time using HEIMDALL,[2] while the 10 cm data were analysed with the package SIGPROC (http://sigproc.sourceforge.net/). No pulsed signal with a period similar to that detected in X-rays, nor single dispersed pulses were found down to a signal-to-noise ratio of 8. Table 4 lists the upper limits obtained at each epoch and frequency.

5 DISCUSSION

Thanks to an intensive *Chandra* and *XMM–Newton* observational campaign of SGR J1935+2154 covering the first eight months since the first bursts detected by *Swift* BAT, we were able to infer the main timing and spectral properties of this newly identified member of the magnetar class. In particular, we discovered strong coherent pulsations at a period of about 3.24 s in a *Chandra* long pointing carried out in 2014 July. Subsequently, by using the *XMM–Newton* observations (spaced so to keep the pulse phase coherence among pointings), we started building a timing solution by means of a phase fitting technique. We were able to phase-connect all the 2014 *Chandra* and *XMM–Newton* data sets and we inferred both a first and second period derivative. These findings further confirm that SGR J1935+2154 is indeed a magnetar which is slowing-down at a rate of about half a millisecond per year. However, this trend is slowing-down due to a negative $\ddot{P}$ (see Table 2). The accurate timing solution allowed us also to infer the dipolar magnetic field strength, an upper limit on the true pulsar age and the corresponding spin-down luminosity (under usual assumptions).

SGR J1935+2154 is a seemingly young object, ≤3 kyr, with a B_p value (∼2.2 × 10^{14} Gauss) well within the typical range of magnetars. The X-ray emission is pulsed. The pulse shape is energy independent (within uncertainties) and it is almost sinusoidal with a ∼20 per cent pulsed fraction (measured as the semi-amplitude of the sinusoid divided by the average count rate) during 2014. It becomes less sinusoidal with a pulsed fraction of only 5 per cent during the latest *XMM–Newton* observation. We detected an energy-dependent phase shift (∼0.16 cycles at maximum), with the hard photons anticipating the soft ones. This behaviour is not very common among known magnetars, 1RXS J1708−4009 being a notable exception (though with a different trend in energy; see Israel et al. 2001; Rea et al. 2005). In 1RXS J1708−4009 the shift is likely associated with the presence of a (spin phase) variable hard X-ray component extending up to at least 100 keV (Kuiper et al. 2006; Götz et al. 2007). Similarly, the pulse profile phase shift of SGR J1935+2154 might be due to the presence of at least two distinct components (peaks) with different weight at different energies. The non-detection of emission from SGR J1935+2154 at energies above 10 keV does not allow us to firmly assess the cause of the shift.

The source spectrum can be well described by the canonical two-component model often applied to magnetars, i.e. an absorbed BB plus a PL (kT∼0.5 keV and Γ ∼2). The SGR J1935+2154 1–10 keV observed flux of 1.5 × 10^{-12} erg cm^{-2} s^{-1} is among the lowest observed so far from magnetars at the beginning of their outbursts. Although it is possible that we missed the outburst onset (which perhaps occurred before the first burst epoch), a backward search of burst activity in the BAT data at the position of SGR J1935+2154 gave negative results (Cummings & Campana 2014). Emission from SGR J1935+2154 is detected in an archival *Swift* XRT pointing in 2011 at a flux only a factor of few lower than the one detected soon after the burst emission. At current stage, we cannot exclude that the source has not reached the quiescent level or that it has a relatively bright quiescent luminosity. This latter possibility is partially supported by the unusual properties of SGR J1935+2154 which displays both intervals of flux weakening and brightening superimposed to a slow decay. We note that the latest *XMM–Newton* pointing occurred less than 20 d from the Konus-*Wind* detection of the first intermediate flare from this source (Golenetskii et al. 2015; Kozlova et al. 2016).

A significant diffuse emission, extending from spatial scales of >1 arcsec up to more than 1 arcmin around the magnetar was clearly detected both by *Chandra* and *XMM–Newton*. Due to the use of different instruments/modes at different epochs, we were not able to test if the diffuse component varied in time (as expected in the case of scattering by dust clouds on the line-of-sight) between the *Chandra* and *XMM–Newton* pointings. Among the *XMM–Newton* pointings, the component does not change significantly. The *Chandra* data allowed us to sample the spatial distribution of the component only up to about 20 arcsec (at larger radii we are hampered by the statistics), while the lower spatial resolution of the *XMM–Newton* pn allowed us to detect the diffuse emission only beyond about 20 arcsec. We do not detect any flux variation for the diffuse emission among the eight *XMM–Newton* pointings despite the pulsar enhancement of

[2] see http://sourceforge.net/projects/heimdall-astro/ for further details.

about 20 per cent between 2014 October and 2015 March, a result which would favour a magnetar wind nebula (MWN) interpretation. The PL model used to fit the pn spectra implies a relatively steep photon index of about 3.8 which is similar to what observed for the candidate MWN around Swift J1834−0846 (Younes et al. 2012), but at the same time is steeper than the PL photon index of SGR J1935+2154 suggesting that the dust scattering scenario might be more likely.

In Swift J1834−0846, two diffuse components have been identified: a symmetric component around the magnetar extending up to about 50 arcsec interpreted as a dust scattering halo (Younes et al. 2012; Esposito et al. 2013), and an asymmetric component extending up to 150 arcsec proposed as a wind nebula (Younes et al. 2012). The spectrum of the former component has a PL photon index steeper than that of the magnetar (which however, at variance with SGR J1935+2154, is fitted well by a single PL alone likely due to a very high absorption which hampers the detection of any soft BB), while the latter has a flatter spectrum. In order to compare the properties of the diffuse emission around Swift J1834−0846 and SGR J1935+2154, we fitted the *Chandra* and *XMM–Newton* spectra of SGR J1935+2154 with a PL alone obtaining a photon index of 4.4 ± 0.1 and 4.3 ± 0.1 (we used only photons in the 1.5–8.0 keV band similar to the case of Swift J1834−0846) implying that the diffuse component might have a spectrum flatter than that of the magnetar and favouring the wind nebula scenario. In the latter case, the efficiency at which the rotational energy loss of a pulsar, $\dot{E}_{\rm rot}$, is radiated by the PWN is given by $\eta_{\rm X} = L_{\rm X,pwn}/\dot{E}_{\rm rot} = (0.6 \times 10^{34}/1.7 \times 10^{34}) \simeq 0.35$, not that different from what inferred from similar components around Swift J1834−0846 and RRAT J1819−1458 (Rea et al. 2009b; Younes et al. 2012). Further *XMM–Newton* and/or *Chandra* observations taken at flux levels significantly different from those we recorded so far should help in settling the nature of the diffuse emission.

A search for radio pulsed emission from SGR J1935+2154 gave negative result down to a flux density of about 0.5 mJy (and 70 mJy for a single pulse). It has been suggested that whether or not a magnetar can also shine as a transient radio pulsar might depend on the ratio between its quiescent X-ray luminosity and spin-down luminosity, given that all magnetars with detected radio pulsed emission have this ratio smaller than ∼0.3 (Rea et al. 2012), at variance with typical radio-quiet magnetars that have quiescent X-ray luminosity normally exceeding their rotational power. Based on the coherent timing solution, we inferred a spin-down luminosity of about 2×10^{34} erg s^{-1}. At the present stage, it is also rather difficult to obtain a reliable value of the quiescent luminosity due to the uncertainties on the distance and the flux of the *Swift* pre-burst detection. If a distance of 9 kpc is assumed, the *Swift* faintest flux convert to a luminosity of about 5×10^{33} erg s^{-1}which results in $L_{\rm X}/L_{\rm sd} \sim 0.25$, close to the 0.3 limiting value. However, if the distance is larger and/or the quiescent flux is a factor of few larger than estimated from *Swift*, the source would move towards higher values of $L_{\rm X,\,qui}/L_{\rm sd}$ in the 'radio-quiet' region of the Fundamental Plane (see left-hand panel of figure 2 in Rea et al. 2012). Correspondingly, the non-detection of radio pulsations might be not that surprising.

The uncertainty in the quiescent level of this new magnetar makes any attempt to infer its evolutionary history rather uncertain. Given the short characteristic age (a few kyrs, which is most probably representative of the true age given that no substantial field decay is expected over such a timespan), the present value of the magnetic field is likely not that different from that at the moment of birth. The above reviewed timing characteristics would then be consistent with a quiescent bolometric luminosity of the order of $\sim 5 \times 10^{33-34}$ erg s^{-1} (see figs 11 and 12 in Viganò et al. 2013), depending on the assumed magnetic field geometry and envelope composition.

Constraints on its outburst luminosity evolution can be put from general considerations (see Pons & Rea 2012; Viganò et al. 2013). If we assume that the flux derived by the pre-outburst *Swift* observations provides a correct estimate of the magnetar quiescence, and we rely on a distance of 9 kpc, then the source luminosity increases from a quiescent level of $L_{\rm X,\,qui} \sim 7 \times 10^{33}$ erg s^{-1} to a 'detected' outburst peak of $L_{\rm X,\,out} \sim 4 \times 10^{34}$ erg s^{-1}. Such luminosity variation within the outburst (about a factor of 5) is rather small for a magnetar with a medium-low quiescent level (see fig. 2 of Pons & Rea 2012). In particular, the outburst peak luminosity usually reaches about $L_{\rm X,\,out} \sim 5 \times 10^{35}$ erg s^{-1}, due to the typical energies released in magnetars' crustal fractures (about 10^{44-45} erg; Perna & Pons 2011; Pons & Rea 2012), coupled with estimates of the neutrino cooling efficiencies (Pons & Rea 2012). If there are no intrinsic physical differences between this outburst and other magnetar outbursts (see Rea & Esposito 2011), then we can foresee two possibilities to explain the relatively low maximum luminosity detected.

The first possibility is that we have missed the real outburst peak of SGR J1935+2154, which was then caught already during its outburst decay. In this case, the quiescent luminosity claimed by the archival *Swift* observation might be correct, and the magnetar had a flux increase during the outburst, but we could catch it only thanks to an SGR-like burst detected when the magnetar had already cooled down substantially. Given the typical outburst cooling curves, we can roughly estimate that, in this scenario, we observed the source about 10–40 d after its real outburst onset.

The second possibility is that the source distance is farther than the assumed SNR distance of 9 kpc (note that the method used by Pavlović et al. 2013 to infer this distance implies a relatively large degree of uncertainty, even a factor of 2 in both directions). To have an outburst peak luminosity in line with other magnetars, SGR J1935+2154 should have a distance of ∼20–30 kpc. At this distance, the assumed *Swift* quiescence level would also be larger ($\sim 7 \times 10^{34}$ erg s^{-1}), hence a factor of ∼5 in increase in luminosity in the outburst would then be in line with what observed (and predicted) in other cases (see again fig. 2 of Pons & Rea 2012). However, in the direction of SGR J1935+2154, the Galaxy extends until ∼14 kpc (Hou, Han & Shi 2009) making such a large distance rather unlikely.

We then suggest that the very low peak flux of the detected outburst of SGR J1935+2154 has no different physics involved with respect to other magnetar outbursts, but we have simply missed the onset of the outburst. If the flux detected by *Swift* before the outburst was its quiescent level, we envisage that the outburst onset occurred about a month before the first X-ray burst detection. If further observations will set the source at a lower quiescent level, the outburst peak should have occurred even longer before we first detected its activity.

ACKNOWLEDGEMENTS

The scientific results reported in this article are based on observations obtained with the *Chandra X-ray Observatory* and *XMM–Newton*, an ESA science mission with instruments and contributions directly funded by ESA Member States and NASA. This research has made use of software provided by the *Chandra* X-ray Center (CXC) in the application package CIAO, and of

softwares and tools provided by the High Energy Astrophysics Science Archive Research Center (HEASARC), which is a service of the Astrophysics Science Division at NASA/GSFC and the High Energy Astrophysics Division of the Smithsonian Astrophysical Observatory. This research is based on observations with the NASA/UK/ASI *Swift* mission. We thank N. Schartel for approving the *XMM–Newton* 2014 November observation through the Director's Discretionary Time program and the staff of the *XMM–Newton* Science Operation Center for performing the Target of Opportunity observations. Similarly, we thank B. Wilkes for approving the *Chandra* 2014 August observation through the Director's Discretionary Time program and the *Chandra* staff for performing the Target of Opportunity observations. We thank the *Swift* duty scientists and science planners for making these observations possible. The Parkes radio telescope is part of the Australia Telescope which is funded by the Commonwealth of Australia for operation as a National Facility managed by CSIRO. The authors warmly thank Phil Edwards for the prompt scheduling of the observations and John Reynolds for releasing part of the telescope time of his project. We thanks Jules Halpern for useful comments. NR is supported by an NWO Vidi Grant, and by grants AYA2012-39303 and SGR2014-1073. This work is partially supported by the European COST Action MP1304 (NewCOMPSTAR).

REFERENCES

Albano A., Turolla R., Israel G. L., Zane S., Nobili L., Stella L., 2010, ApJ, 722, 788
Arnaud K. A., 1996, in Jacoby G. H., Barnes J., eds, ASP Conf. Ser. Vol. 101, Astronomical Data Analysis Software and Systems V. Astron. Soc. Pac., San Francisco, p. 17
Burgay M., Israel G. L., Rea N., Possenti A., Zelati F. C., Esposito P., Mereghetti S., Tiengo A., 2014, Astronomer's Telegram, 6371, 1
Burrows D. N. et al., 2005, Space Sci. Rev., 120, 165
Camero-Arranz A. et al., 2013, MNRAS, 429, 2493
Camilo F., Ransom S. M., Halpern J. P., Reynolds J., Helfand D. J., Zimmerman N., Sarkissian J., 2006, Nature, 442, 892
Campana S., de Ugarte Postigo A., Thoene C. C., Gorosabel J., Rea N., Coti Zelati F., 2014, GRB Coordinates Netw., 16535, 1
Cummings J. R., Campana S., 2014, Astronomer's Telegram, 6299, 1
Cummings J. R., Barthelmy S. D., Chester M. M., Page K. L., 2014, Astronomer's Telegram, 6294, 1
De Luca A., Molendi S., 2004, A&A, 419, 837
Duncan R. C., Thompson C., 1992, ApJ, 392, L9
Esposito P. et al., 2013, MNRAS, 429, 3123
Golenetskii S. et al., 2015, GRB Coordinates Netw., 17699
Götz D. et al., 2007, A&A, 475, 317
Granet C. et al., 2005, IEEE Antennas Propag. Mag., 47, 13
Hou L. G., Han J. L., Shi W. B., 2009, A&A, 499, 473
Israel G., Oosterbroek T., Stella L., Campana S., Mereghetti S., Parmar A. N., 2001, ApJ, 560, L65
Israel G. L., Rea N., Zelati F. C., Esposito P., Burgay M., Mereghetti S., Possenti A., Tiengo A., 2014, Astronomer's Telegram, 6370, 1
Kozlova A. et al., 2016, MNRAS, submitted
Kuiper L., Hermsen W., den Hartog P. R., Collmar W., 2006, ApJ, 645, 556
Paczynski B., 1992, Acta Astron., 42, 145
Pavlović M. Z., Urošević D., Vukotić B., Arbutina B., Göker Ü. D., 2013, ApJS, 204, 4
Perna R., Gotthelf E. V., 2008, ApJ, 681, 522
Perna R., Pons J. A., 2011, ApJ, 727, L51
Pons J. A., Rea N., 2012, ApJ, 750, L6
Rea N., Esposito P., 2011, in Torres D. F., Rea N., eds, Astrophys. Space Sci. Proc., Vol. 21, High-Energy Emission from Pulsars and their Systems. Springer, Heidelberg, p. 247
Rea N., Oosterbroek T., Zane S., Turolla R., Méndez M., Israel G. L., Stella L., Haberl F., 2005, MNRAS, 361, 710
Rea N. et al., 2009a, MNRAS, 396, 2419
Rea N. et al., 2009b, ApJ, 703, L41
Rea N. et al., 2010, Science, 330, 944
Rea N., Pons J. A., Torres D. F., Turolla R., 2012, ApJ, 748, L12
Rea N. et al., 2013, ApJ, 770, 65
Read A. M., Rosen S. R., Saxton R. D., Ramirez J., 2011, A&A, 534, A34
Stamatikos M., Malesani D., Page K. L., Sakamoto T., 2014, GRB Coordinates Netw., 16520, 1
Staveley-Smith L. et al., 1996, Publ. Astron. Soc. Australia, 13, 243
Stil J. M. et al., 2006, AJ, 132, 1158
Strüder L. et al., 2001, A&A, 365, L18
Sun X. H., Reich P., Reich W., Xiao L., Gao X. Y., Han J. L., 2011, A&A, 536, A83
Surnis M. P., Krishnakumar M. A., Maan Y., Joshi B. C., Manoharan P. K., 2014, Astronomer's Telegram, 6376, 1
Turner M. J. L. et al., 2001, A&A, 365, L27
Turolla R., Zane S., Pons J. A., Esposito P., Rea N., 2011, ApJ, 740, 105
Viganò D., Rea N., Pons J. A., Perna R., Aguilera D. N., Miralles J. A., 2013, MNRAS, 434, 123
Weisskopf M. C., Tananbaum H. D., Van Speybroeck L. P., O'Dell S. L., 2000, in Truemper J. E., Aschenbach B., eds, Proc. SPIE Conf. Ser. 4012, X-Ray Optics, Instruments, and Missions III. SPIE, Bellingham, p. 2
Wilms J., Allen A., McCray R., 2000, ApJ, 542, 914
Younes G., Kouveliotou C., Kargaltsev O., Pavlov G. G., Göğüş E., Wachter S., 2012, ApJ, 757, 39

This paper has been typeset from a TEX/LATEX file prepared by the author.